Geochemistry, Geophysics, Geosystems®

AGU ADVANCING EARTH AND SPACE SCIENCES

RESEARCH ARTICLE
10.1029/2023GC011286

Automated Detection and Machine Learning-Based Classification of Seismic Tremors Associated With a Non-Volcanic Gas Emission (Mefite d'Ansanto, Southern Italy)

S. Panebianco[1,2], C. Satriano[3], G. Vivone[1], M. Picozzi[4], A. Strollo[5], and T. A. Stabile[1]

[1]National Research Council of Italy (CNR-IMAA), Tito Scalo, Italy, [2]Now at Department of Physics and Earth Sciences, University of Ferrara, Ferrara, Italy, [3]Université Paris Cité, Institut de physique du globe de Paris, CNRS, Paris, France, [4]Department of Physics, University of Naples, Naples, Italy, [5]GFZ German Research Centre for Geoscience, Potsdam, Germany

Key Points:

- A dense temporary seismic array enabled the acquisition of emission-related seismic tremor at the Mefite d'Ansanto site
- A detection algorithm and supervised machine-learning approach for the identification and classification of tremors has been developed
- New insights on the emission tremor would help to monitor the CO_2 degassing at the Mefite d'Ansanto and its temporal evolution

Supporting Information:

Supporting Information may be found in the online version of this article.

Correspondence to:

S. Panebianco,
serenapanebianco@cnr.it

Citation:

Panebianco, S., Satriano, C., Vivone, G., Picozzi, M., Strollo, A., & Stabile, T. A. (2024). Automated detection and machine learning-based classification of seismic tremors associated with a non-volcanic gas emission (Mefite d'Ansanto, Southern Italy). *Geochemistry, Geophysics, Geosystems*, *25*, e2023GC011286. https://doi.org/10.1029/2023GC011286

Received 13 OCT 2023
Accepted 21 JAN 2024
Corrected 2 MAR 2024

This article was corrected on 2 MAR 2024. See the end of the full text for details.

Author Contributions:

Conceptualization: S. Panebianco, C. Satriano, G. Vivone, T. A. Stabile
Data curation: M. Picozzi, A. Strollo
Formal analysis: S. Panebianco
Funding acquisition: T. A. Stabile
Investigation: S. Panebianco, C. Satriano, M. Picozzi, A. Strollo

Abstract A major aim in the study of crustal fluids is the development of automatic methodologies for monitoring deep-source, non-volcanic gas emissions' spatio-temporal evolution. Crustal fluids play a significant role in the generation of large earthquakes and the characterization of their emissions on the surface can be essential for better understanding crustal processes generating earthquakes. We investigate seismic tremors recorded over 4 days in 2019 at the Mefite d'Ansanto (southern Apennines, Italy) that is located at the northern end of the fault system that generated the Mw 6.9 1980 Irpinia Earthquake. The Mefite d'Ansanto is hypothesized to be the largest natural, non-volcanic, CO_2-rich gas emission on Earth. The seismic tremor is studied by employing a dense temporary seismic network and an automated detection algorithm based on non-parametric statistics of the recorded signal amplitudes. We extracted signal characteristics (RMS amplitude and statistical moments of amplitudes both in time and frequency domains) for use in the subsequent supervised machine-learning classification of the target tremor and accidently detected anthropogenic and background noise. The data set is used for the training and optimization of station-based KNN (k-Nearest-Neighbors) binary classifiers obtaining good classification performances with a median overall accuracy across all stations of 92.8%. The classified tremor displayed common features at all stations: variable duration (16 s to 30–40 min), broad peak frequency (4–20 Hz) with varying amplitudes, and two types of signals: (a) long-duration, high-amplitude tremor and (b) pulsating tremor. Higher tremor amplitudes recorded at stations closer to local bubbling and pressurized vents suggest multiple local tremor sources.

1. Introduction

Seismic tremor in volcanic areas is an extensively studied phenomenon due to its recognized association with the volcanic activity and its role in forecasting incipient eruptions as well as in understanding the interaction between magmatic fluids and the surrounding rocks (e.g., Saccorotti & Lokmer, 2021; Zuccarello et al., 2022). Recent works demonstrated that the characterization of seismic tremor in volcanic gas emissions areas (e.g., fumarolic vents) is a powerful tool to monitor volcanic unrest related to hydrothermal activity and for risk mitigation (among others, Chiodini et al., 2017; Giudicepietro et al., 2019). Conversely, studies on seismic tremor arising from gas emissions are less frequent (La Rocca et al., 2023; Morabito et al., 2023). Nevertheless, quantifying seismic tremor has great potential in shedding light on the geodynamics of complex, tectonic degassing regions as well as in monitoring the close relationship between seismic activity and deep fluid discharge. Non-volcanic gas emissions are often located in tectonically active areas, where deep fluid circulation and ascent is enabled by fault systems and highly fractured rocks (Caracausi & Paternoster, 2015; Chiodini et al., 2004, 2020). The role of fluid pore pressure in earthquake triggering is now widely recognized (Miller et al., 2004; Shapiro, 2015; Stabile et al., 2021; Tamburello et al., 2018). Developing methodologies for reconstructing the spatio-temporal evolution of non-volcanic gas emissions seismic tremor is therefore essential to better understand large earthquake generation processes. Both in volcanic and in non-volcanic settings, standard approaches for tremor monitoring and characterization are mainly based on manual analyses of seismic signals both in the time and frequency domain. However, with the growing amount of data continuously acquired by dense monitoring seismic networks, manual inspection of signals needs to be integrated with automatic and/or machine learning (ML) tools. As a result, recent research has focused on the implementation of automatic tools for real-time tremor analysis with seismic array techniques (Smith & Bean, 2020) and/or in the application of both supervised and unsupervised machine learning

Methodology: S. Panebianco, C. Satriano, G. Vivone, T. A. Stabile
Project administration: T. A. Stabile
Resources: M. Picozzi, A. Strollo
Software: S. Panebianco, C. Satriano
Supervision: C. Satriano, G. Vivone, T. A. Stabile
Validation: S. Panebianco, C. Satriano, G. Vivone, T. A. Stabile
Visualization: S. Panebianco
Writing – original draft: S. Panebianco, T. A. Stabile
Writing – review & editing: S. Panebianco, C. Satriano, G. Vivone, M. Picozzi, A. Strollo, T. A. Stabile

approaches for tremor characterization and classification (Curilem et al., 2017; Malfante et al., 2018; Masotti et al., 2008; Permana et al., 2022).

In this work, we investigated seismic tremors recorded at the Mefite d'Ansanto emission site (Figure 1). The site, known since the 5th century BC (Di Lisio et al., 2014), is renowned as the largest natural emission on Earth of non-volcanic, CO_2-dominated gases, with an estimated daily gas flux of approximately 2,000 tons (Chiodini et al., 2010). Situated in the Irpinia area (Figure 1), the Mefite d'Ansanto site lies within one of the highest seismic hazard areas in Europe: the Southern Apennines. Extensional processes involve the axial zone of the chain since the Middle-Late Pleistocene and up to 15 km deep NW–SE striking faults have developed that can generate M7 earthquakes (Mw 6.9, 1980 Irpinia Earthquake—Bernard & Zollo, 1989) and along with the gas leakage occurs. Mefite d'Ansanto developed at the northern end of the fault system activated by the Irpinia earthquake (Figure 1) in the well-known thermal anomaly area of Mt. Forcuso (Festa et al., 2021; Improta et al., 2014). The emission is fed by a 1,128 to 1,600 m-deep CO_2 gas reservoir encountered by a 1,850 m deep well drilled at about 2 km east (Monte Forcuso 001 well, ViDEPI Project, 2012). The nature of the deep source of this CO_2-dominant (98 vol%, Chiodini et al., 2010) gas manifestation have been widely discussed (Buttitta et al., 2023; Caracausi & Paternoster, 2015; Caracausi et al., 2013; Chiodini et al., 2004). At the surface, the emission extends over an area of about 4,000 m^2 (Chiodini et al., 2010) and occurs mainly as diffuse soil degassing with local bubbling pools and pressurized vents, mainly oriented SW along a fault zone along which a river flows, as evidenced also by the lack of vegetation in the area (Figure 1).

The Mefite d'Ansanto was studied in terms of seismic wavefield polarization from ambient noise measurements (Pischiutta et al., 2013). More recently, the seismic tremor recorded here from seismic arrays was characterized in time-frequency domains (La Rocca et al., 2023; Morabito et al., 2023). Morabito et al. (2023) found the seismic tremor is characterized by higher amplitudes in four main frequency bands (0.2–1 Hz; 1–5 Hz; 5–10 Hz; 10–15 Hz); La Rocca et al. (2023) described three main kinds of signals in the emission area which were classified in terms of their frequency content and amplitude as follows: (a) low-frequency, low-amplitude tremor; (b) high frequency pulses of low amplitude and very short duration; (c) intermediate-frequency tremor with sudden amplitude variations. The latter type of wavefield is defined as a persistent intermediate-frequency (3–20 Hz) tremor that is hypothesized being associated with a shallow source within the emission area, and it has been described as a stable amplitude tremor (weak tremor) interested by a non-stationary increase in signal amplitude (strong tremor) (La Rocca et al., 2023). The aim of this study was to develop and test an automated machine-learning workflow to detect and classify strong tremor events in the Mefite d'Ansanto area. We performed a quantitative analysis of the wavefield recorded by a temporary dense seismic array deployed at the Mefite d'Ansanto emission area (Figure 1). The use of a dense seismic array allowed the inclusion of signals having a high signal-to-noise ratio. First, we developed a strategy for the automated detection of strong tremor (hereafter referred to as: "tremor") based on non-parametric statistics of the recorded amplitudes at each station of the array. Then, for each station, we trained a supervised machine learning (KNN–k-nearest neighbors, Cover & Hart, 1967) classification algorithm using typical tremor features to discriminate it from other recorded signals (e.g., "low energy tremor," here simply defined as "background noise" and/or anthropic spikes). After a brief description of the dense seismic array deployed in the emission area, the automated and machine-learning methods applied in this work are described in detail. Finally, the automated approach performance is discussed along with the main observations about the signals classified as tremor.

2. The Mefite d'Ansanto Seismic Array

The seismic wavefield at Mefite d'Ansanto was characterized by a temporary dense seismic network (FDSN network code: YZ_2017, Passarelli et al., 2017) installed at the emission site between 28 October 2019 and 05 November 2019 by the German Research Center for Geoscience (GFZ) as part of a temporary experiment (East Pollino Experiment, Southern Italy, Passarelli et al., 2017). The aim of the experiment was to monitor the interaction between crustal fluids and earthquake occurrence. The dense seismic array was installed around the emission site and consisted of 11 surface seismic stations (Figure 1 and Table 1). The maximum and minimum inter-station distances were 340 and 60 m, respectively, with a maximum height difference of 44 m. Two kinds of triaxial seismometers were installed: (a) 4 broad-band sensors (Trillium Compact 120 s) installed at stations R01B, R07B, R08B, and RSFI; (b) 7 short-period passive sensors (SM-6 4.5 Hz) installed at stations R02S, R03S, R04S, R05S, R06S, R10S, and R11S. Continuous waveform recordings were acquired by the YZ network with CUBE data loggers using a sampling rate of 200 Hz.

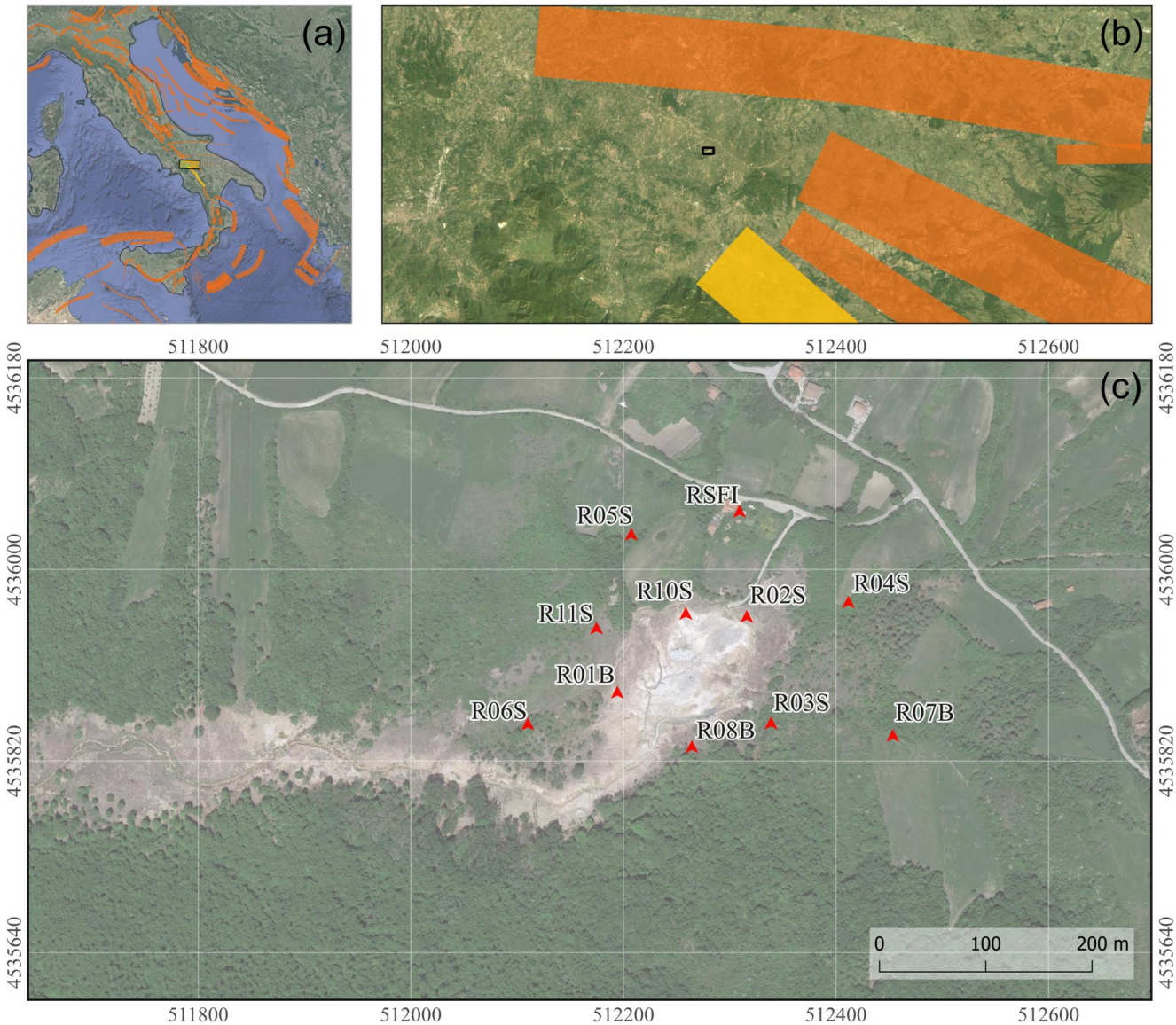

Figure 1. The Mefite d'Ansanto gas emission location in the Irpinia area (Campania Region, Italy). (a) and (b) Seismogenic sources related to the Irpinia Fault System are indicated by the yellow rectangle; other potential sources for large earthquakes in the area are indicated in orange (Database of Individual Seismogenic Sources, DISS, Version 3.3.0 2021). (c) Zoom of the emission site, recognizable from the lack of vegetation, and the location of the 11 seismic stations of the temporary array.

3. Time-Frequency Characteristics of Tremor

We analyzed the continuous data streams from broadband (R01B, R07B, R08B, and RSFI) and short-period (R02S, R03S, R04S, R05S, R06S, R10S, R11S) stations in the period between 30 October 2019 and 2 November 2019 during which all the 11 stations were in operation. The time-frequency visualization of the background seismicity recorded at Mefite d'Ansanto enabled us to observe non-stationary signals characterized by the emergent onset of seismic tremor marked by (Figure 2): (a) higher amplitudes with respect to the background noise (b) variable duration (from tens of seconds to tens of minutes); (c) prominent spectral peaks in the frequency range 4–20 Hz; (d) an emergent onset, almost simultaneous across all stations due to the small inter-station distance; (e) no preferential occurrence in either daytime or night time (Figure 4).

The tremor spectral content at both broadband and short period stations presents three main characteristics (Figure 3a): (a) the amplitude spectra are characterized by different peaks in the frequency range 4–20 Hz, (b) the latter peaks show a different dominant frequency and/or different relative amplitude from station to station, (c) the

Table 1
Station Locations, Characteristics, and Installation Times of the Mefite d'Ansanto Array

Station ID	Network	Lon (DD)	Lat (DD)	Elevation(m)	Sampling rate (Hz)	Sensor	Installed	Uninstalled
R01B	YZ_2017	15.1448	40.9740	709.80	200	Trillium Compact 120 s	28/10/2019 00:00	04/11/2019 00:00
R02S	YZ_2017	15.1463	40.9747	727.35	200	SM-6 4.5 Hz	28/10/2019 00:00	05/11/2019 00:00
R03S	YZ_2017	15.1466	40.9738	714.44	200	SM-6 4.5 Hz	29/10/2019 00:00	05/11/2019 00:00
R04S	YZ_2017	15.1474	40.9748	725.86	200	SM-6 4.5 Hz	29/10/2019 00:00	05/11/2019 00:00
R05S	YZ_2017	15.1450	40.9754	727.27	200	SM-6 4.5 Hz	29/10/2019 00:00	05/11/2019 00:00
R06S	YZ_2017	15.1438	40.9738	703.04	200	SM-6 4.5 Hz	29/10/2019 00:00	05/11/2019 00:00
R07B	YZ_2017	15.1479	40.9737	722.37	200	Trillium Compact 120 s	29/10/2019 00:00	05/11/2019 00:00
R08B	YZ_2017	15.1457	40.9736	704.83	200	Trillium Compact 120 s	28/10/2019 00:00	05/11/2019 00:00
R10S	YZ_2017	14.1456	40.9747	715.45	200	SM-6 4.5 Hz	29/10/2019 00:00	05/11/2019 00:00
R11S	YZ_2017	15.1446	40.9746	718.60	200	SM-6 4.5 Hz	29/10/2019 00:00	05/11/2019 00:00
RSFI	YZ_2017	15.1462	40.9756	748.54	200	Trillium Compact 120 s	28/10/2019 18:01	05/11/2019 16:30

spectral content beyond 20 Hz exhibits significant variation across different stations, likely due to local propagation and site effects. Looking at tremor spectral content in the broadband stations (R01B, R07B, R08B, and RSFI), spectral peaks at 0.2–0.5 Hz and a minor peak at 3 Hz are also recognizable. These low frequency peaks can be consistently observed also in the frequency content of the background noise across different stations. Therefore, the latter cannot be considered to be part of the seismic tremor of interest but rather classified as environmental seismic noise. In addition, two monofrequency peaks at 1.5 and 50 Hz can be observed on unsmoothed spectra of some stations, which can be attributed to wind turbines and electric current, respectively. The background noise spectral content (Figure 3b), which appears highly variable across different stations due to local propagation effects, shows distinct features. Indeed, it appears to be characterized by higher dominant frequencies and/or different peaks compared to tremors. The observed attributes of tremor events, both in terms of time and frequency domain, emphasize the significance of extracting features from both waveforms and spectral content for the discrimination of tremor events from noise and other kinds or recorded signals.

4. Methods

Since the observed peculiarities of signals vary from station to station both in time and frequency content, we applied a station-based automated detection and machine learning classification approach, which involves two main steps: (a) an automatic detection algorithm (ADA) for the preliminary identification of potential tremors in the background noise and for the extraction of their characteristic parameters (i.e., RMS-amplitude and statistical moments); (b) the application of the a k-nearest neighbors (KNN) classifier at each station—trained with the previously extracted parameters as features—for a more robust, automatic tremor discrimination.

4.1. Automated Detection Algorithm (ADA) and Features Extraction

Exploiting the Mefite array continuous recordings, we implemented an automated detection algorithm (ADA) through Python-ObsPy (Krischer et al., 2015) seismic signal processing tools (Figures 4 and 5) to extract the

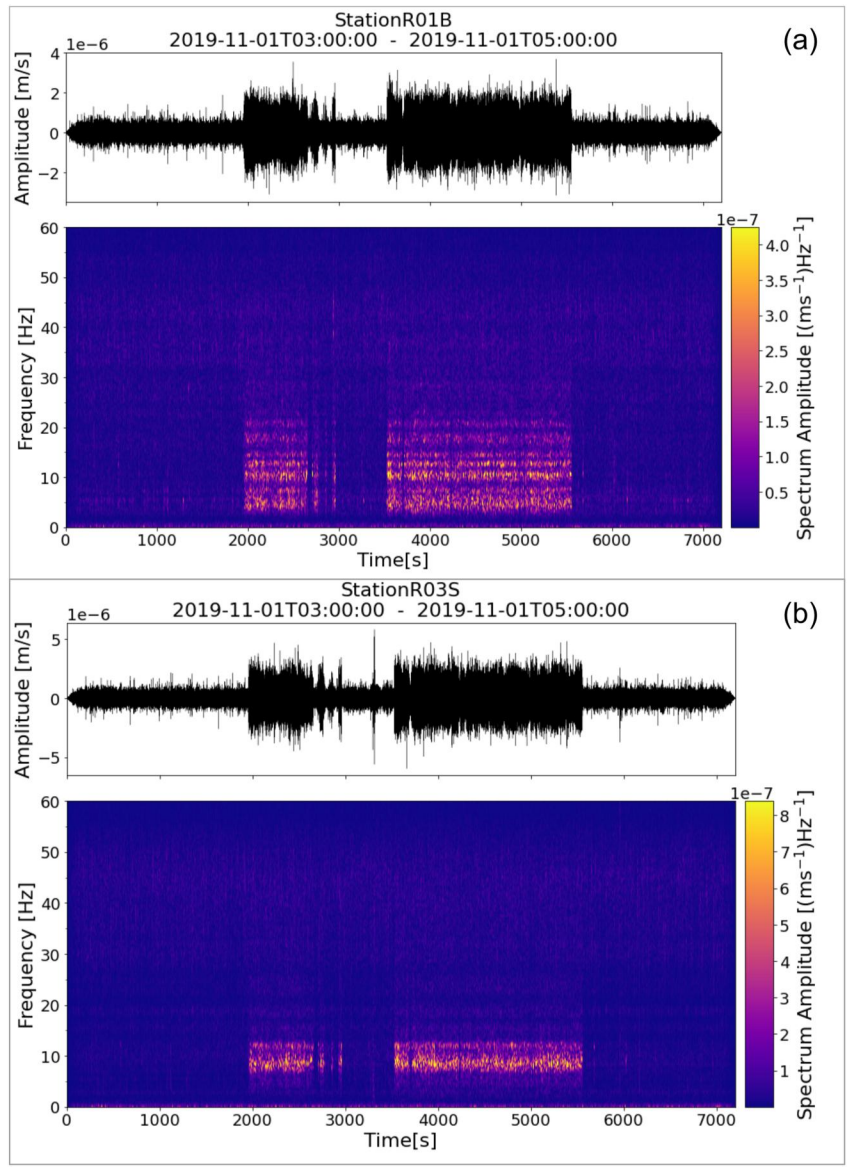

Figure 2. Two-hour long vertical component seismograms and their relative spectrograms at (a) R01B broadband and (b) R03S short-period stations. A 0.1 Hz high pass filter was applied to exclude the effects of low frequency seismic noise on records.

typical characteristics of signals. The algorithm is based on non-parametric statistics of the recorded amplitudes at each station and was applied only to vertical signal components to minimize problems related to local site amplifications. The detection is performed through the following steps (Figure 4): (a) the traces are bandpass filtered in the frequency range where the higher amplitudes were observed across all stations (6–15 Hz) to enhance the tremor onset over the record; (b) the smoothed envelopes of the signals are calculated; (c) tremor start- and end-times are measured as the times when the envelope goes above and below, respectively, a given threshold. After some tuning analysis we applied a centered moving average function for the smoothing of the signal envelope (with length of 3,000 points, which corresponds to a 15 s window), since it resulted the most effective smoothing window in the tremor identification scheme. For a more robust statistical choice of detection amplitude threshold, we made no assumption on the amplitude's statistical distributions and estimated it as the 90th percentile of the recorded absolute amplitude distribution. This enabled us to set data-driven thresholds for each analyzed day (Figure S1 in Supporting Information S1). Both the threshold estimation and the tremor detection methods were applied on amplitudes expressed in counts, since the conversion in the physical unit is not essential in this step.

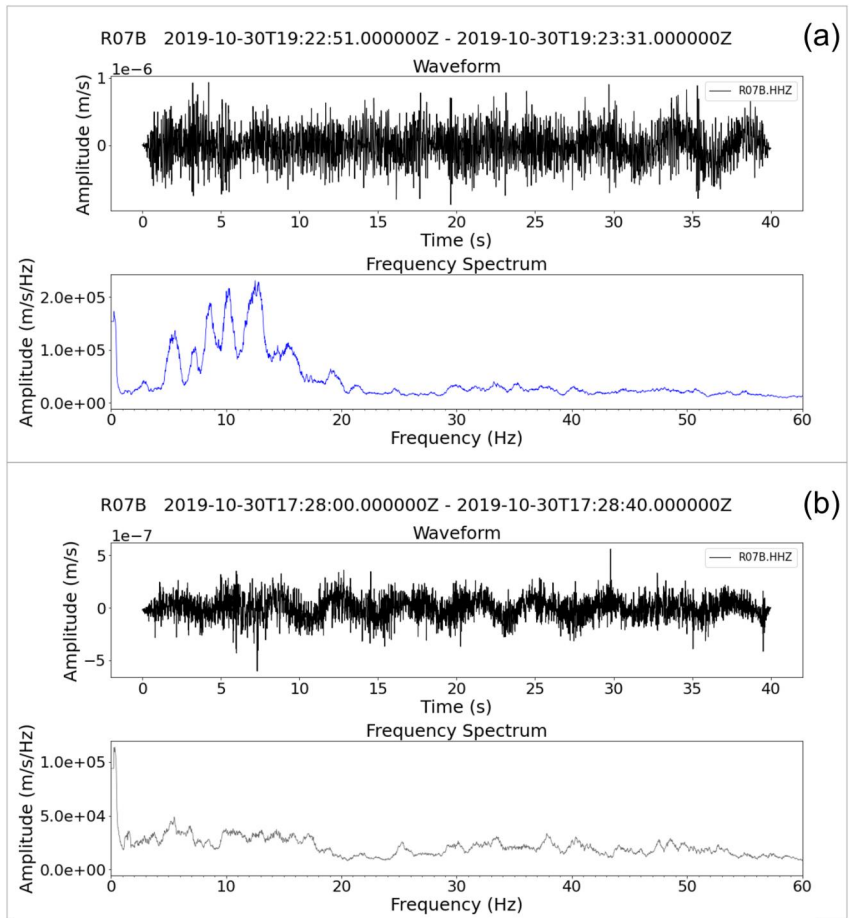

Figure 3. Comparison of spectral content between (a) a 40 s-long tremor event and (b) a 40 s-long noise window recorded at station R07B within the same hour. For both signals, the image shows the waveform and the frequency spectrum. The latter is windowed between 0 and 60 Hz (since no significant spectral content was observed for higher frequencies) and slightly smoothed with a central moving average (over 15 points) to highlight the main spectral peaks without excessively masking the actual spectral content.

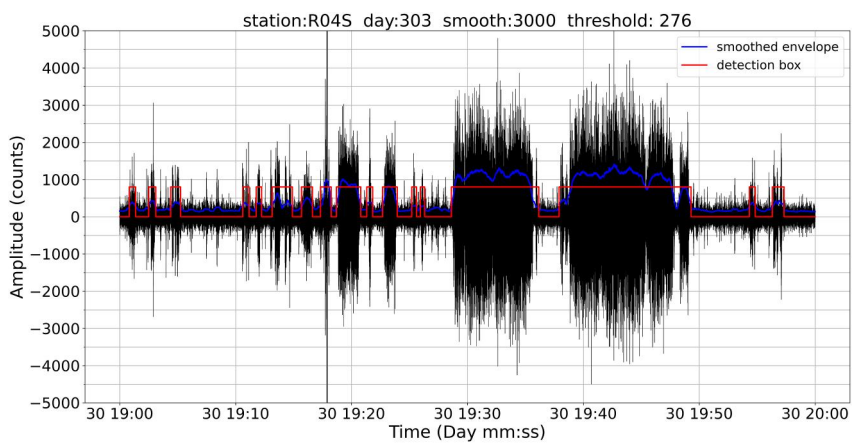

Figure 4. An example of the detection algorithm workflow applied to a 1-hr signal (19:00:00–20:00:00 UTC time) recorded on 30 October 2019 (Julian day 303) at station R04S. First, the smoothed envelope of the 6–15 Hz filtered waveform (blue curve) is calculated; then, event detection is performed through a box function (red curve) which assumes non-zero values for envelope amplitudes greater than the threshold (276 counts).

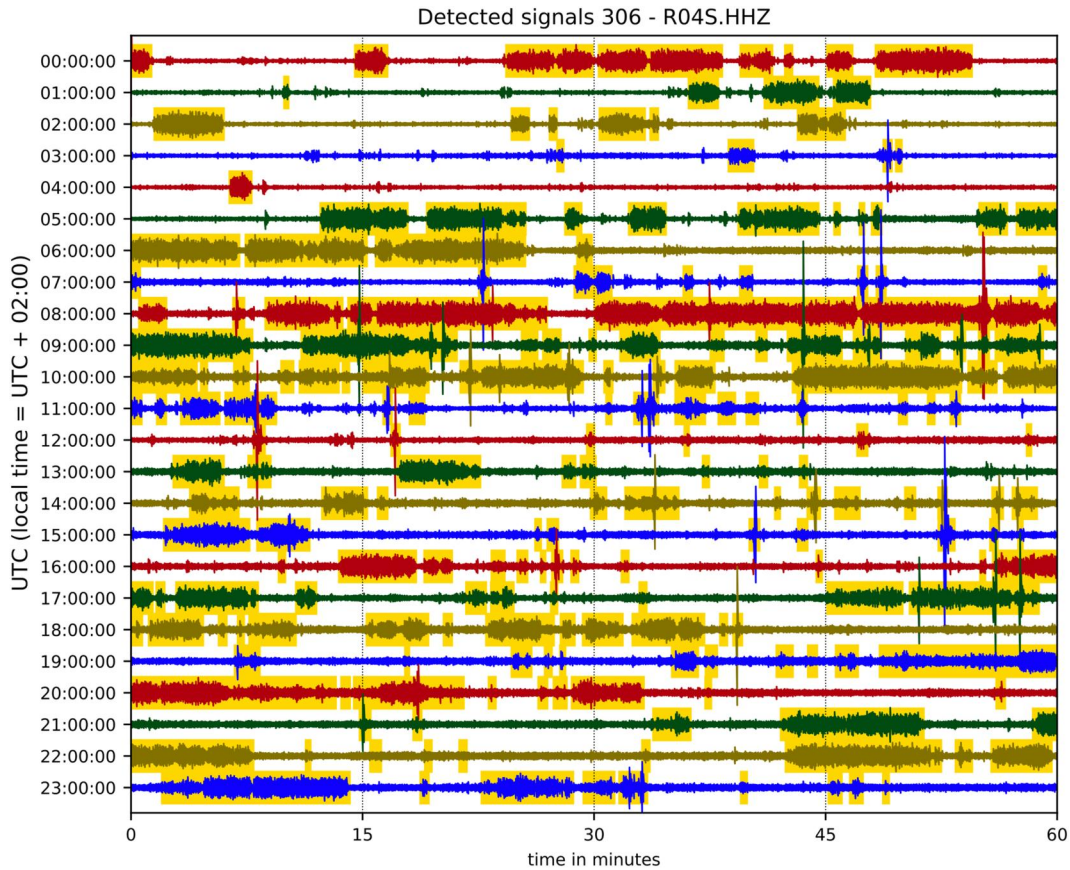

Figure 5. Helicorder display showing the ADA detection results at station R04S on 02 November 2019 (Julian day 306). Each yellow bar on the plot corresponds to the signal automatically detected by our algorithm.

We applied the ADA detector on the R04S station waveforms recorded from 30 October 2019 to 2 November 2019. Indeed, this station was positioned approximately at the midpoint between the emission area and a road, making it well-suited for capturing not only emission-related signals but also a valuable selection of anthropic signals. In the assumption of seismic tremors propagating from common sources and the previous observations of signals recorded almost simultaneously across the stations (Section 3, Figure 2), we collected signal features for each station, using the same time windows (the same start and end times) of ADA detections performed on R04S station. This operation was carried out either to leverage the close deployment of the array or because it would also be valuable for the subsequent comparison of the station-based classifier performances. Thus, for each preliminary detection time window and for all the stations, we extracted signal characteristic parameters to obtain an alternative representation (feature domain) with respect to the original one (temporal domain). For each preliminary identified tremor, the following parameters (features) were estimated: (a) the RMS ground velocity amplitude (m/s) of the 6–15 Hz bandpass-filtered and instrument-deconvolved signal; (b) the statistical moments (mean, standard deviation, skewness, and kurtosis) of the raw signal amplitude distributions in both time and frequency domains (Figure 6). The first parameter describes the signal in terms of its average amplitude (m/s). The latter parameters describe the signal shape: the standard deviation describe the spread of data around the mean value, the skewness shows the asymmetry of the signal as a distribution with respect to a Gaussian one, and the kurtosis reflecting its flatness and the number of outliers in it (Curilem et al., 2017; Malfante et al., 2018).

4.2. Feature Selection

The preliminary application of the ADA algorithm allowed the extraction of signal features for tremor ML classification. Only the features which better represent signals should be selected to suitably train a given classifier to correctly define the decision space (assigning a classification label). The aim of feature selection is to identify truly relevant features—or feature combinations –for the task at hand, and eventually discard the

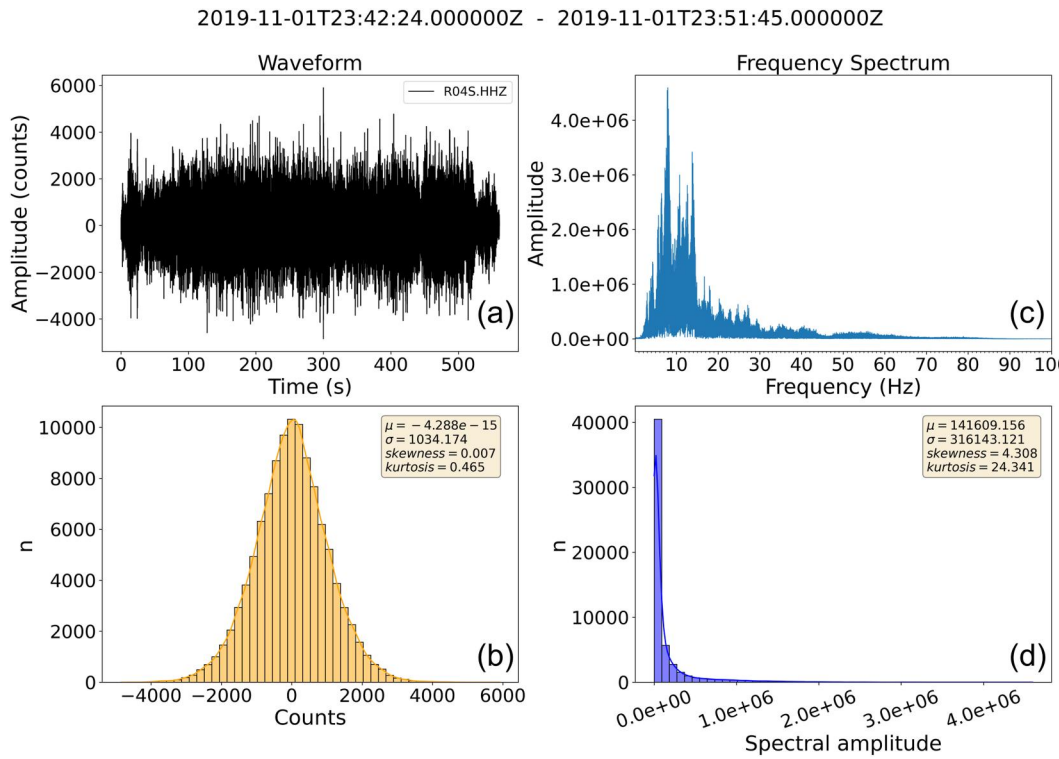

Figure 6. An example of statistical features extracted from a preliminary identified tremor. The amplitude distributions in both time (a, b) and frequency (c, d) are analyzed to extract the 1st (mean), 2nd (standard deviation), 3rd (skewness), and 4th (kurtosis) statistical moments.

irrelevant and redundant ones (Hall, 2000). This step is important in the application of the KNN algorithm, which classifies each signal using all the available features in distance computations (see Section 4.3). We selected a subset of 45 signal samples from the R04S station (vertical component) comprising 15 tremor events, 15 noise windows, and 15 anthropic spikes (Table S1 in Supporting Information S1). We estimated for all the 45 signals the previously defined features (RMS amplitude and statistical moments of amplitude distributions in both time and frequency domains). Looking at their bivariate relationships (Figure 7a) and linear correlations (Figure 7b), we excluded the mean of spectral amplitudes as a feature for classifier training given its high linear correlation ($r = 0.96$) and high standard deviation. The latter has typically lower values for the noise, while kurtosis and skewness of tremors spectral amplitude distributions generally showed smaller variability with respect to non-tremor signals (noise and spikes). Despite its high linear correlation with kurtosis ($r = 0.94$), the skewness of spectral amplitudes was kept in the feature space since it helped the classifiers improve their performance. Furthermore, the mean of signal amplitudes in the time domain was excluded since it was not useful in the discrimination of tremors from background noise. This is due to the prior application of a 6–15 Hz bandpass filter to the signals during the analysis; thus, both tremors and background noise have zero-mean. In this respect, the standard deviation was a useful feature, while the skewness and the kurtosis values typically discriminate anthropic spikes. Lastly, we kept the RMS amplitude because the signal amplitude was already used in the previous preliminary ADA detection step. The final 7 selected features (RMS amplitude; standard deviation, skewness, kurtosis of amplitude distributions in time domain; standard deviation, skewness, kurtosis of amplitude distributions in the frequency domain) are summarized in Table S2 of the Supporting Information S1.

4.3. KNN Classification of Tremor Signals

To perform an automatic robust detection and discrimination of tremor events we applied a supervised machine learning approach. Thus, we implemented a binary classification with the k-nearest neighbor algorithm (Cover & Hart, 1967). KNN is a widely used classifier because of its nonparametric nature and for its conceptual simplicity. As a supervised machine learning algorithm, it relies on labeled input data (training data) to learn a function

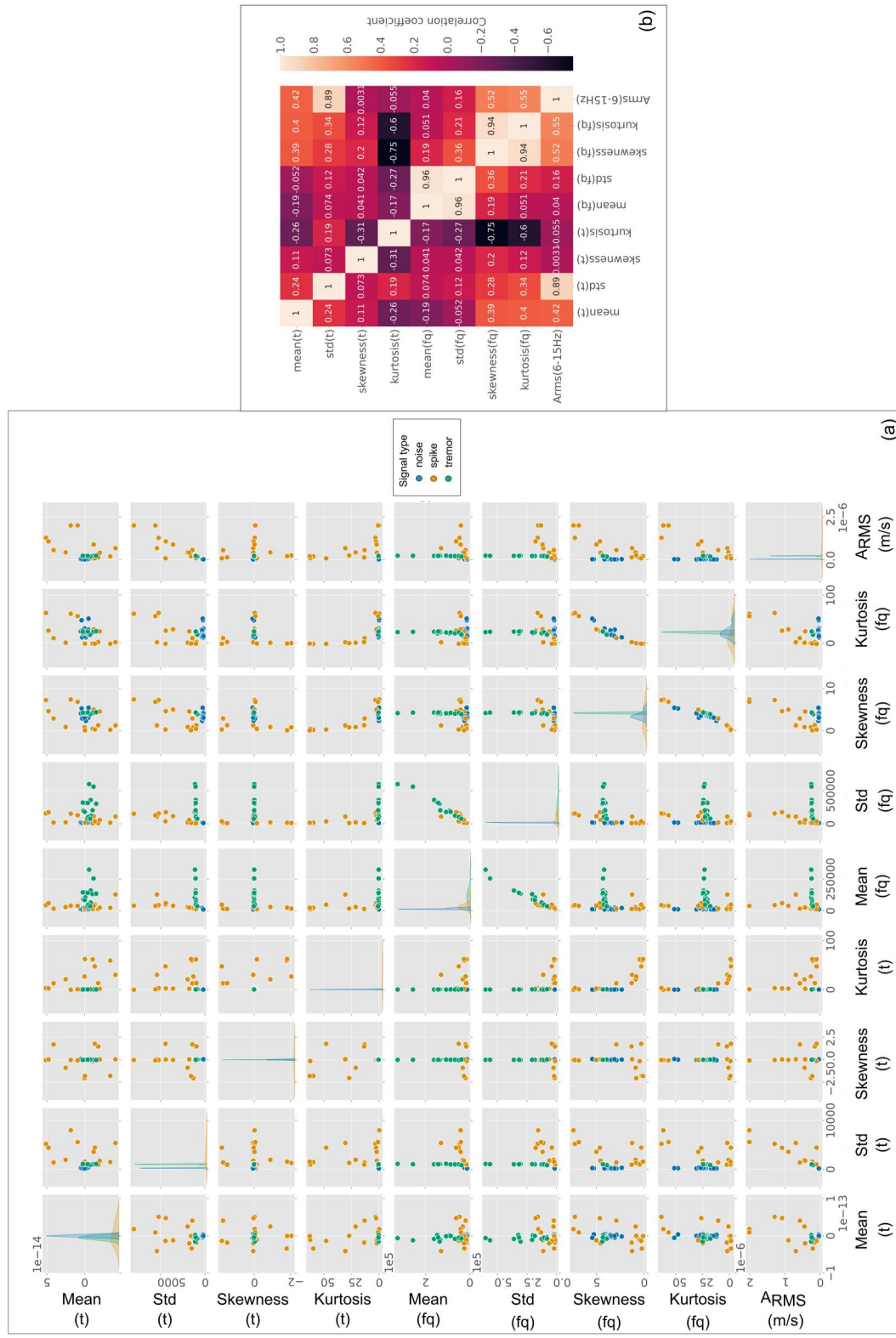

Figure 7. Summary of features collected for the 45 samples signals used for signal selection: (a) pairplot showing the bivariate correlations and kernel density estimate (over the main diagonal) for the different types of signals: tremors (green dots), noise (blue dots) and anthropic spikes (orange dots); (b) correlation matrix showing the linear correlation between each couple of features expressed in terms of Pearson's coefficient (r).

(model) that can be then used to classify unlabeled data. A KNN classification is based on feature similarity, measured as the distance from several K labeled points (nearest neighbors). We chose the Euclidean distance as the similarity metrics. The number K is the core deciding factor (hyperparameter) of the algorithm: each data point will get the most recurring label amongst its closest K points. The algorithm was implemented through the Python-scikit-learn machine learning module (Pedregosa et al., 2011).

Given the observed station-related peculiarities of the recorded waveforms and tremor events both in the time- and frequency domains (Section 3), we performed station-based classifier training, thus obtaining 11 station - specific KNN classifiers. We first standardized features to avoid misleading training and classification results related to different parameters scale. Then, for the KNN model training, we used the same signals for all the stations selected through visual inspection and time-frequency analyses. A total training data set of 481 events (246 tremor—class 0; 253 no-tremor—class 1) recorded in the first three analyzed days (30–31 October 2019 and 1st November 2019) was used. The non-tremor class comprised both background noise and anthropic spike samples. We randomly chose 80% of the observations to train the model. The remaining 20% of the labeled observations were used for testing. We performed an accuracy K cross-validation. Considering that the K-values should be odd for an even number of classes (Kim, 2012) (here: tremor signal, non-tremor signal) we generated different KNN models for different K-values and for each station we selected the classifier which would produce the maximum classification overall accuracy. Finally, for further validation of the generalization properties of the selected KNN models, we evaluated their binary classification performance on a new data set characterized by differing features of signals with respect to those in the training set. For this purpose, we used for each station the same 199 signals which were selected between the ADA detections on the last analyzed day (02-11-2019) of the array records.

5. Results and Discussion

5.1. Classification Performances

The application of the preliminary tremor detection approach (i.e., ADA algorithm) showed some limitations given the intrinsic difficulty in discriminating between tremor and other signals (e.g., anthropic spikes) based solely on the amplitude of the recorded waveforms which, in turn, could lead to underestimation and incomplete characterization of the tremor in the degassing area. However, the preliminary detection technique enabled us to collect a large starting data set of 917 signals for each station which allowed for KNN's training and testing. On the other hand, the application of the supervised KNN binary classification allowed us to overcome the ADA limitations and to better discriminate tremor events with respect to other wrongly detected signals (e.g., anthropic spikes) with more efficient signal representation (feature domain). The classifiers were trained with features (RMS amplitude and statistical moments) extracted for the signals retrieved at the same time-windows at individual stations. Then, for each station, the classification was performed. Among the stations, the K-values are comprised mainly between 3 and 7. The overall low K-values reflect models that are well constrained based on the training data in defining the decision boundaries for classification. However, low K values can also make the models more sensitive to outliers or mislabeled data points and more affected by possible generalization issues due to overfitting. The classifier performances in terms of the main binary classification metrics are summarized in Table 2. We evaluated the performance of the KNN model at each station through the confusion matrix, which contains the main information about the distribution of samples within the predicted classes. In its general definition, the confusion matrix is a square matrix ($G \times G$) whose rows and columns represent the experimental and predicted classes, respectively (Ballabio et al., 2018). In the case of a binary classification, it is a (2×2) matrix defined by the total number of accurate predictions—True Positives (TP) and True Negatives (TN)—and the total number of misclassifications—False Positives (FP) and False Negatives (FN). The elements of a confusion matrix are used to evaluate different metrics about the classifier performances. We considered accuracy, precision, recall, and F1-score (Lever et al., 2016). The overall accuracy represents the number of correctly classified data instances over the total number of data instances; the precision (or positive predictive value) considers both TP and FP instances and represents the accuracy of the positive prediction; while the recall (also known as sensitivity or true positive rate) is the measure of the proportion of known positives that are predicted correctly (TPs). Finally, the F1-score is defined as the harmonic mean of the precision and recall, a single metric combining both measures into a balanced evaluation. All these classification metrics range from 0 (bad classifier) to 1 (good classifier). For each station, we report the optimized KNN results in terms of their respective metrics (Figure 8).

Table 2
Summary of the K Values Selected Through Cross-Validation Along With the Classification Performance of the Corresponding KNN Model at Each Station

Station	K	Recall	Precision	F1-score	Accuracy
R01B	3	0.915	0.896	0.905	0.907
R02S	5	0.872	0.911	0.891	0.897
R03S	13	0.894	0.955	0.923	0.928
R04S	1	0.872	0.911	0.891	0.897
R05S	3	0.872	0.976	0.921	0.928
R06S	7	0.894	0.977	0.933	0.938
R07B	13	0.83	0.813	0.821	0.825
R08B	15	0.936	0.978	0.957	0.959
R10S	3	0.957	0.938	0.947	0.948
R11S	7	0.894	0.955	0.923	0.928
RSFI	7	0.915	0.896	0.905	0.907

Looking at the classification metrics for all the stations (Table 2, Figure 8), the KNN classifiers show good classification performances with a median overall accuracy between all the stations of 0.928 (92.8%). The maximum overall accuracy of 0.959 (95.9%) was reached by the R08B station classifier, while the minimum performance (82.5%) was found for the R07B station. The high accuracy indicates that the KNN models predicted the correct class labels for a large portion of the instances for most stations. Considering the median values of other metrics across all stations (recall: 0.738; precision: 0.940; F1-score: 0.827), the KNN models are conservative in classifying instances as positive, resulting in a higher number of false negatives. The generally lower recall values of the KNN models suggests that the model is not as effective at correctly identifying all the positive instances from the data set, which can be related to the presence of mislabeled data (e.g., noise-contaminated tremors or tremor-contaminated noise) in the training data set. In turn, the higher precision values suggest that if the models classify an instance as positive, it is likely to be correct. These observations reflect the intrinsic trade-off between the recall and precision metrics (Buckland & Gey, 1994), in turn evaluated from the F1-score. The station at which the KNN shows the lower F1-score of 0.719 is R06S, while we found the maximum trade-off between precision and recall at the R07B station (F1-score: 0.886). The median value of 0.827 (82.7%) between all stations indicates a reasonable balance between precision and recall, and hence a good overall performance of the station KNNs. Classifier metrics confirm that the station-based training approach, even if more time consuming, is an effective strategy to reliably train the KNN to discriminate between tremor events and other signals wrongly detected using the ADA algorithm.

To further validate the optimized KNN classifiers and their generalization performances, we applied it to a different data set with respect to the one used for training and testing. Again, we performed the classification for each station, evaluating their performance on a labeled dataset made of 199 signals selected between the ADA detections on the last analyzed day (02-11-2019) of the array records. To better compare the results, we considered for each station the same signals. As expected, we obtained a decrease in the overall KNN's performance across all stations of about 10% with an estimated median value of overall accuracy of 82.9%. The trained KNN models are capable of correctly classifying a high percentage of events. The observed decrease in performance is likely due to the KNN's sensitivity to data distribution and mis-labeled data in the training phase and to the algorithm intrinsic limitations in terms of generalization due to its non-parametric nature

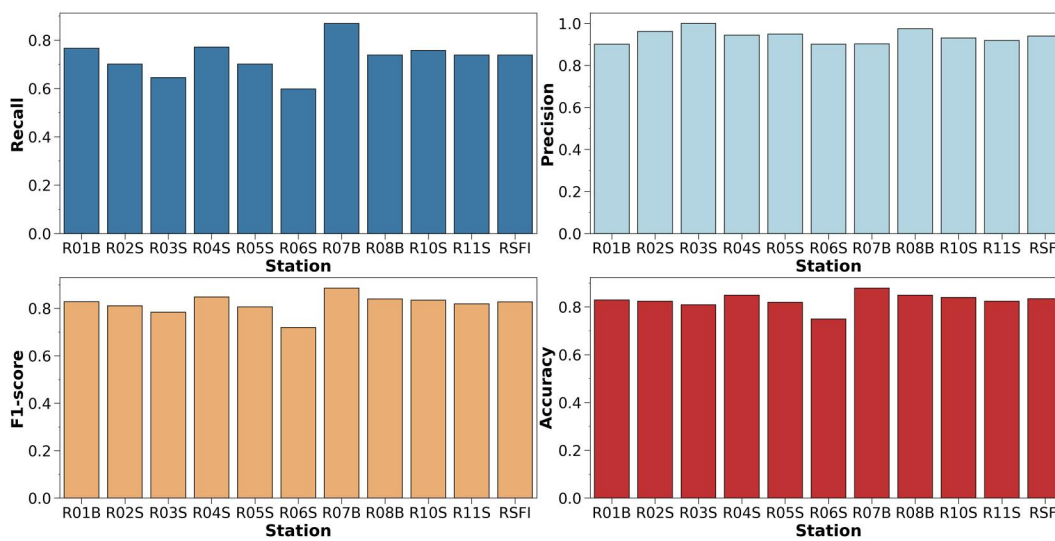

Figure 8. Classification metrics (Recall, Precision, F1-Score, Accuracy) estimated for the validation of each station-trained KNN classifier.

(Cover & Hart, 1967). Overall, the observed decrease in generalization capacity, although expected on a different data set from the one used for the algorithm training and testing, suggests the need to further explore machine learning approaches and algorithms in the future to improve this first-order application for the automatic seismic tremor classification at Mefite d'Ansanto.

5.2. Classified Signal Characterization

As a first-order ensemble approach, we used a majority voting technique to combine the results of the 11 independent single-station KNN classifications of the new data set—used to assess the generalization properties of the algorithms—to define the final class prediction of its signals. This approach can help to mitigate the impact of individual model biases and to obtain a more robust and accurate prediction of tremor events. We have assumed an equal weight for each model at this stage and at the end of the procedure simply assigned to each signal the class label that appeared most frequently in the independent single-station classifications. Over the total 199 events of the analyzed data set, 117 were classified as tremor (class 0) by major voting, while 82 were classified as

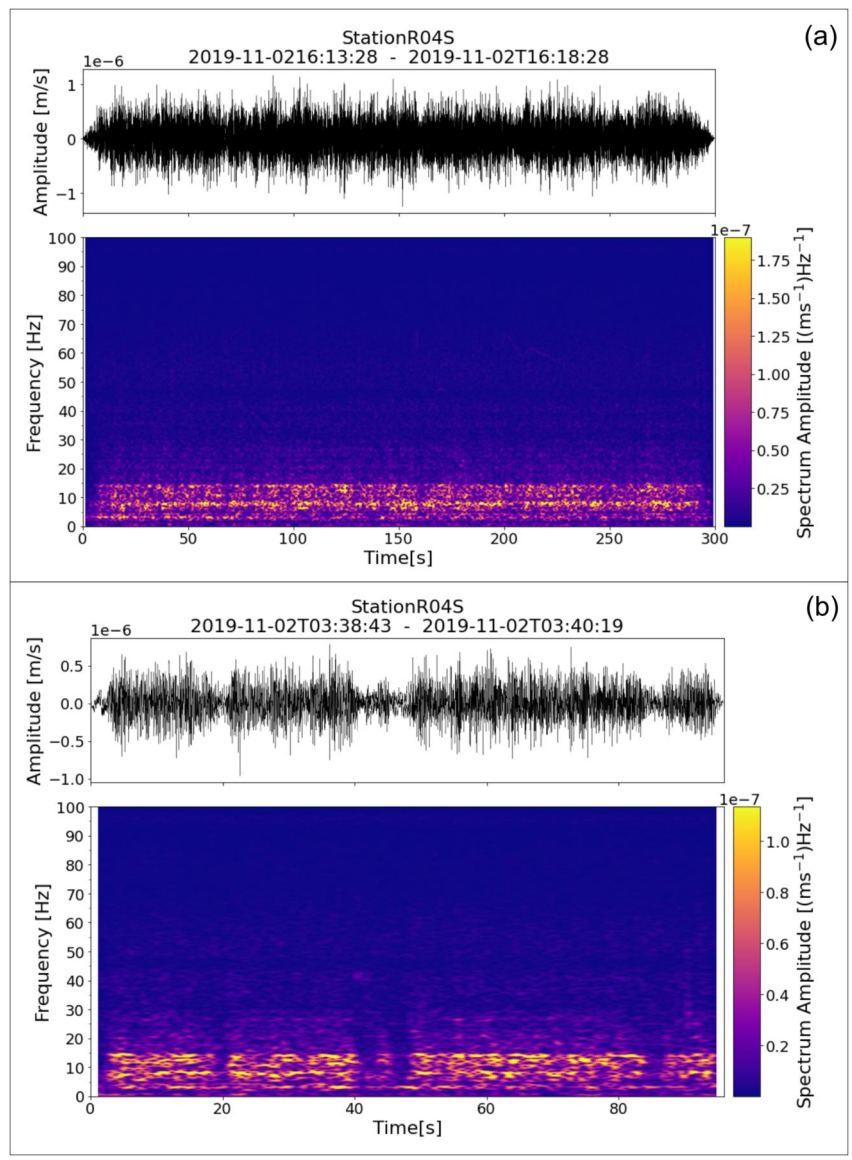

Figure 9. Two main kinds of signal classified as tremors (class 0) after major voting recorded from the R04S station are (a) long tremors (>100 s) generally characterized by higher amplitudes and (b) pulsating tremor made by sequences of closely spaced short tremors of a few seconds.

no-tremor (class 1) mainly comprising anthropic spikes, accidently detected background noise, and minor tremors embedded in the background noise (Table S3, Figure S2 in Supporting Information S1). These latter signals have a duration generally less than 100 s (median value 33.5s) with RMS amplitudes generally smaller than the classified tremor. Moreover, their amplitude distributions include numerous outliers, indicating that these signals vary from station to station with inconsistent patterns (Figure 10b). On the other hand, tremor duration is highly variable, ranging from tens of seconds (minimum duration 16 s) to tens of minutes (maximum duration 2,270 s). Two main kinds of tremor signals were observed: (a) long-duration tremor (>100 s) generally characterized by higher amplitudes (Figure 9a); (b) pulsating tremor made of sequences of closely spaced short tremor signals of a few seconds (Figure 9b). Both types of signals occur with no specific patterns and with no daily preferential distribution (Figure S3 in Supporting Information S1). The alternation of impulsive and long tremors is similar to that described by Hsu et al. (2013) related to intermittent emission of gas by active mud volcanoes and to the so-called spasmodic and pulsating tremors associated with ash and gas emissions of intermediate energy (Arámbula-Mendoza et al., 2016). The signal's spectral content shows similarities with that of continuous fumarolic tremor (Chiodini et al., 2010; Giudicepietro et al., 2019), which is characterized by a spectral peak in a narrow frequency band around 10 Hz. Different from fumaroles, the examined tremor displays a wider range of frequencies,

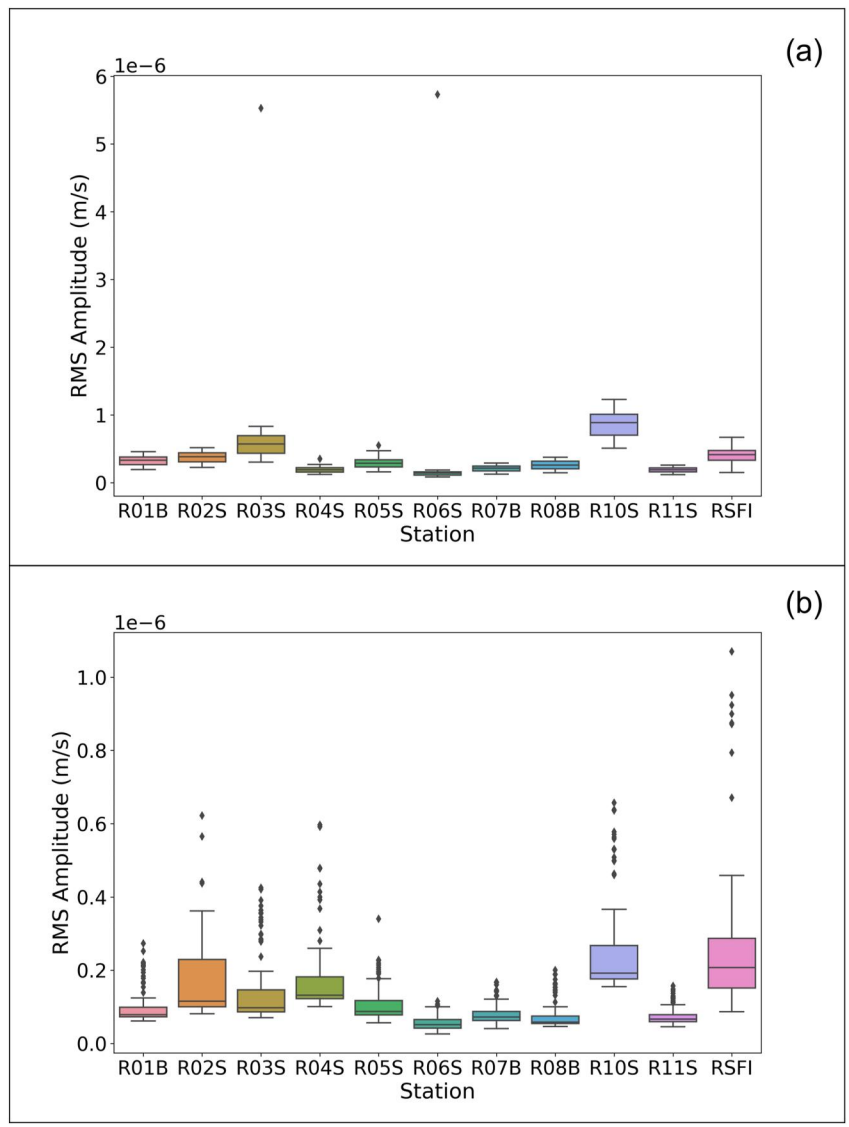

Figure 10. Box Plot representation of the RMS-amplitude (m/s) distributions (6–15 Hz bandpass filtered waveforms) at each station of the array estimated for (a) the classified tremor (class 0) and (b) the classified non-tremor (class 1) signals.

typically between 4 and 20 Hz. Within this range, its peak frequency values and amplitudes are affected by local propagation characteristics at each station. Different source-related effects in the gas emission area are likely characterized by multiple and diffuse potential tremor sources (gas vents, water bubbling), which together with the local morphology cause peculiar spectral patterns at each station.

Comparing the amplitude distributions of the same signals at different stations (Figure 10a), the classified tremor RMS amplitudes (6–15 Hz) showed the same order of 10^{-7} m/s across the stations. Their distributions are mainly symmetric and characterized by few outliers, thus suggesting that classified data exhibit a relatively consistent pattern and supporting the assumption that we are observing the same signal across different stations within the same time-windows, as assumed before. We can also observe that higher amplitude values are recorded by the inner stations of the array (R10S, R03S R02S, R01B), that is, those closer to the emission area. Exceptions are the external stations RSFI and R05S, whose high amplitudes might be related to a smaller and isolated gas emission placed to the NW of the main emission area (i.e., the area with reduced vegetation right above station R05S in Figure 1). These amplitude observations indicate local tremor sources within the Mefite d'Ansanto emission area. The highest signal amplitudes were recorded at the R10S station (median value of 8.88×10^{-7}), the closest to the bubbling pools (Figure 10a), and at R03S (median value of 5.7×10^{-7}), the closest to one pressurized vent located at the southeastern side of the emission area identified during on-site investigations (Panebianco, 2022). These qualitative observations along with amplitude variability across the array stations would agree with the hypothesis of different emission sources (e.g., bubbling water, pressurized vents) existing in the Mefite d'Ansanto area in accordance with the results of array analysis performed by La Rocca et al. (2023) on the "intermediate frequency tremor," of which the tremor events under analysis would be partly ascribable.

6. Conclusion

In this work, we developed a first-order automated and machine-learning workflow to detect and classify hydrothermal tremor events recorded in the Mefite d'Ansanto non-volcanic gas emission area. The extraction of new information about the Mefite D'Ansanto seismic tremor was made possible by the installation of a dense seismic array around the emission site, which allowed the recording of continuous high-resolution data at 11 different stations. The workflow involved (a) the implementation of an amplitude-based automatic detection algorithm (ADA) at one station, which enabled the preliminary identification of potential tremors and the contextual extraction of feature characteristics; and (b) the training of station-based k-nearest neighbors (KNN) binary classifiers with selected features to perform a robust and automatic tremor discrimination. The initial application of the tremor detection approach (ADA algorithm) revealed limitations, mainly due to the challenge of distinguishing tremor from other signals (e.g., anthropic spikes) based solely on the amplitude of recorded waveforms. Nevertheless, this preliminary detection technique yielded a substantial data set of 917 signals for each station, which was used for the subsequent training and testing station-based KNN algorithms. In turn, the implementation of these binary classifiers proved to be a significant improvement over the ADA limitations in tremor discrimination. The single station trained KNN classifiers—applied over the same signals recorded at different stations—showed good classification performances with a median overall accuracy of 92.8%. To further confirm the effectiveness of the optimized K-nearest neighbors (KNN) models, we evaluated their performance on a different labeled data set. To ensure a fair comparison, we used the same signals for each station. The purpose was to assess how well the trained KNN models could generalize to unfamiliar data. The results showed a decrease in the overall accuracy across all stations of 10% (value), which is likely due to the non-parametric nature of the KNN algorithm inherently limiting its generalization ability. The good classification performances indicate the efficacy of the chosen amplitude and statistic features in representing the target signals. The applied supervised machine learning approach enabled us to more reliably and automatically discriminate tremor events from other falsely identified signals (e.g., anthropic spikes). The combined results obtained through majority voting of the same new data set of signals—recorded on 02 November 2019—allowed the definition of the following common characteristics of the classified tremor signals:

1. An emergent onset with amplitudes that become higher with respect to the recorded background noise within a few seconds (Figure 2);
2. Highly variable durations ranging between 16 s and 30–40 min;
3. A similar order of magnitude of RMS amplitudes at all stations of our network (10^{-7} m/s) with local variation at different stations based on their location in the emission area (Figure 10a);

4. A spectral peak in a broad frequency band around 10 Hz with multiple peaks at frequencies in the range 4–20 Hz, whose amplitude locally changes at different stations due to highly variable local propagation and site effects in the emission area;
5. The identified tremors consist of two main types of signals, non-stationary in time and with almost uniform daily distribution (Figure 9, Figure S3 in Supporting Information S1): (a) long duration (>100 s) tremor and (b) pulsating tremor made by sequences of closely spaced short tremors of a few seconds. These characteristics in the time-domain would suggest that tremor events reflect more energetic degassing/bubbling episodes occurring during the continuous gas manifestation (background noise) at Mefite d'Ansanto.

The detected tremor evolution in time (e.g., amplitude variation, pulsating and long-tremor alterations) would represent a useful tool to monitor the massive non-volcanic emission at Mefite d'Ansanto. Moreover, the development in the future of multiparametric, comparative analysis between the detected tremor and physico-chemical parameters (e.g., air CO_2 concentration) would find application in establishing a proxy between tremor events and the quantitative estimation of CO_2 degassing at the site. The higher tremor amplitudes were recorded at stations of the array closer to the emission area (R10S, R03S R02S, and R01B). Particularly, the highest amplitudes were recorded at the R10S station -the closest to the water bubbling pool present in the site- and the R03S station -installed in the vicinity of an energetic pressurized vent- thus suggesting that these two emission manifestations would be the main tremor sources. Our results showing a tremor source internal to the Mefite d'Ansanto emission area are also confirmed by recent findings in the area (e.g., La Rocca et al., 2023; Morabito et al., 2023). However, further development in tremor location should be addressed to confirm these qualitative observations by setting up high-resolution methods (e.g., array techniques) to identify multiple tremor sources (gas vents, water bubbling) over a range of depths.

The automated detection and machine learning-based classification procedure presented in this study has proven to enable the analysis of continuous data streams from different stations without the need for any human intervention. This workflow could be extended to volcanic settings in the future (after appropriate training), enabling the detection, classification, and characterization of volcano-seismic signals for real-time volcano monitoring.

Data Availability Statement

Data used in the creation of this manuscript are available at GEOFON Data Centre at (Passarelli et al., 2017). Automated Detection Algorithm (ADA) version 1.0 (Panebianco et al., 2024) was developed in Python version 3.7.8 with the support of ObsPy version 1.2.2 seismic processing tools (The ObsPy Development Team, 2022). Figures were made with Matplotlib version 3.5.1 (Caswell et al., 2020; Hunter, 2007), available under the Matplotlib license at https://matplotlib.org/. The KNN algorithm was implemented through the Python-scikit-learn machine learning module version 1.0.2 (Grisel et al., 2021; Pedregosa et al., 2011).

Acknowledgments
We are grateful to the local authorities who provided permissions and support during the experiment. We thank the head of the local municipality, F. Lisena, for the expert advice during the deployment as well as G. Lisena for hosting one of the stations for a longer time frame. V. Santoli also supported logistics. Instruments were provided by Section 2.1 and GIPP of the GFZ. We thank H. Woith and L. Passarelli for the realization of the experiment and G. Martinelli for the advice and discussion. We would like to acknowledge the editor, M. Edmonds, and the anonymous reviewers, whose constructive comments allowed us to significantly improve the quality of the manuscript. This research benefited from the financial support of the project "Detection and tracking of crustal fluid by multi-parametric methodologies and technologies" of the Italian PRIN-MIUR program (Grant 20174X3P29).

References

Arámbula-Mendoza, R., Valdés-González, C., Varley, N., Reyes-Pimentel, T. A., & Juárez-García, B. (2016). Tremor and its duration-amplitude distribution at Popocatépetl volcano, Mexico. *Geophysical Research Letters*, *43*(17), 8994–9001. https://doi.org/10.1002/2016GL070227

Ballabio, D., Grisoni, F., & Todeschini, R. (2018). Multivariate comparison of classification performance measures. *Chemometrics and Intelligent Laboratory Systems*, *174*, 33–44. https://doi.org/10.1016/j.chemolab.2017.12.004

Bernard, P., & Zollo, A. (1989). The Irpinia (Italy) 1980 earthquake: Detailed analysis of a complex normal faulting. *Journal of Geophysical Research*, *94*(B2), 1631–1647. https://doi.org/10.1029/JB094iB02p01631

Buckland, M., & Gey, F. (1994). The relationship between recall and precision. *Journal of the American Society for Information Science*, *45*(1), 12–19. https://doi.org/10.1002/(SICI)1097-4571(199401)45:1<12::AID-ASI2>3.0.CO;2-L

Buttitta, D., Capasso, G., Paternoster, M., Barberio, M. D., Gori, F., Petitta, M., et al. (2023). Regulation of deep carbon degassing by gas-rock-water interactions in a seismic region of Southern Italy. *Science of the Total Environment*, *897*, 165367. https://doi.org/10.1016/j.scitotenv.2023.165367

Caracausi, A., Martelli, M., Nuccio, P. M., Paternoster, M., & Stuart, F. M. (2013). Active degassing of mantle-derived fluid: A geochemical study along the Vulture line, southern Apennines (Italy). *Journal of Volcanology and Geothermal Research*, *253*, 65–74. https://doi.org/10.1016/j.jvolgeores.2012.12.005

Caracausi, A., & Paternoster, M. (2015). Radiogenic helium degassing and rock fracturing: A case study of the southern Apennines active tectonic region. *Journal of Geophysical Research: Solid Earth*, *120*(4), 2200–2211. https://doi.org/10.1002/2014JB011462

Caswell, T., Droettboom, M., Lee, A., Hunter, J., Firing, E., Stansby, D., et al. (2020). Matplotlib v3.5.1 [Software]. Zenodo. https://doi.org/10.5281/zenodo.3714460

Chiodini, G., Cardellini, C., Amato, A., Boschi, E., Caliro, S., Frondini, F., & Ventura, G. (2004). Carbon dioxide Earth degassing and seismogenesis in central and Southern Italy. *Geophysical Research Letters*, *31*(7), L07615. https://doi.org/10.1029/2004GL019480

Chiodini, G., Cardellini, C., Di Luccio, F., Selva, J., Frondini, F., Caliro, S., et al. (2020). Correlation between tectonic CO_2 Earth degassing and seismicity is revealed by a 10-year record in the Apennines, Italy. *Science Advances*, *6*(35), eabc2938. https://doi.org/10.1126/sciadv.abc2938

Chiodini, G., Giudicepietro, F., Vandemeulebrouck, J., Aiuppa, A., Caliro, S., De Cesare, W., et al. (2017). Fumarolic tremor and geochemical signals during a volcanic unrest. *Geology*, *45*(12), 1131–1134. https://doi.org/10.1130/G39447.1

Chiodini, G., Granieri, D., Avino, R., Caliro, S., Costa, A., Minopoli, C., & Vilardo, G. (2010). Non-volcanic CO_2 Earth degassing: Case of Mefite d'Ansanto (southern Apennines), Italy. *Geophysical Research Letters*, *37*(11), L11303. https://doi.org/10.1029/2010GL042858

Cover, T., & Hart, P. (1967). Nearest neighbor pattern classification. *IEEE Transactions on Information Theory*, *13*(1), 21–27. https://doi.org/10.1109/TIT.1967.1053964

Curilem, M., Cuevas, A., Soto, R., Huenupan, F., Martin, C. S., Salman Khan, M., et al. (2017). Classification of volcanic seismic events: An expert knowledge analysis for feature selection. In *8th international conference of pattern recognition systems (ICPRS 2017)* (pp. 1–6). https://doi.org/10.1049/cp.2017.0131

Di Lisio, A., Russo, F., & Sisto, M. (2014). La Mefite nella Valle d'Ansanto (Irpinia, Campania): Il valore paradigmatico di un geoarcheosito. *Geologia dell'Ambiente—Italian Magazine of Environmental Geology*, *2–7*.

DISS Working Group. (2021). *Database of individual seismogenic sources (DISS), version 3.3.0: A compilation of potential sources for earthquakes larger than M 5.5 in Italy and surrounding areas*. Istituto Nazionale di Geofisica e Vulcanologia (INGV). https://doi.org/10.13127/diss3.3.0

Festa, G., Adinolfi, G. M., Caruso, A., Colombelli, S., De Landro, G., Elia, L., et al. (2021). Insights into mechanical properties of the 1980 Irpinia fault system from the analysis of a seismic sequence. *Geosciences*, *11*(1), 28. https://doi.org/10.3390/geosciences11010028

Giudicepietro, F., Chiodini, G., Caliro, S., De Cesare, W., Esposito, A. M., Galluzzo, D., et al. (2019). Insight into Campi Flegrei caldera unrest through seismic tremor measurements at Pisciarelli fumarolic field. *Geochemistry, Geophysics, Geosystems*, *20*(11), 5544–5555. https://doi.org/10.1029/2019GC008610

Grisel, O., Mueller, A., Lars, Gramfort, A., Louppe, G., Prettenhofer, P., et al. (2021). scikit-learn/scikit-learn: scikit-learn 1.0.2 (Version 1.0.2) [Software]. Zenodo. https://doi.org/10.5281/ZENODO.5804512

Hall, M. A. (2000). *Correlation-based feature selection of discrete and numeric class machine learning*. (Working paper 00/08). University of Waikato, Department of Computer Science.

Hsu, S.-K., Wang, S.-Y., Liao, Y.-C., Yang, T. F., Jan, S., Lin, J.-Y., & Chen, S.-C. (2013). Tide-modulated gas emissions and tremors off SW Taiwan. *Earth and Planetary Science Letters*, *369*(370), 98–107. https://doi.org/10.1016/j.epsl.2013.03.013

Hunter, J. D. (2007). Matplotlib: A 2D graphics environment. *Computing in Science & Engineering*, *9*(3), 90–95. https://doi.org/10.1109/MCSE.2007.55

Improta, L., De Gori, P., & Chiarabba, C. (2014). New insights into crustal structure, Cenozoic magmatism, CO_2 degassing, and seismogenesis in the southern Apennines and Irpinia region from local earthquake tomography. *Journal of Geophysical Research: Solid Earth*, *119*(11), 8283–8311. https://doi.org/10.1002/2013JB010890

Kim, J. (2012). Department of electrical engineering and computer science. *ACM SIGDA Newsletter*, *20*(1), 91. https://doi.org/10.1145/378886.380416

Krischer, L., Megies, T., Barsch, R., Beyreuther, M., Lecocq, T., Caudron, C., & Wassermann, J. (2015). ObsPy: A bridge for seismology into the scientific Python ecosystem. *Computational Science & Discovery*, *8*(1), 014003. https://doi.org/10.1088/1749-4699/8/1/014003

La Rocca, M., Galluzzo, D., Nardone, L., Gaudiosi, G., & Di Luccio, F. (2023). Hydrothermal seismic tremor in a wide frequency band: The nonvolcanic CO_2 degassing site of Mefite d'Ansanto, Italy. *Bulletin of the Seismological Society of America*, *113*(3), 1102–1114. https://doi.org/10.1785/0120220243

Lever, J., Krzywinski, M., & Altman, N. (2016). Classification evaluation. *Nature Methods*, *13*(8), 603–604. https://doi.org/10.1038/nmeth.3945

Malfante, M., Dalla Mura, M., Metaxian, J.-P., Mars, J. I., Macedo, O., & Inza, A. (2018). Machine learning for volcano-seismic signals: Challenges and perspectives. *IEEE Signal Processing Magazine*, *35*(2), 20–30. https://doi.org/10.1109/MSP.2017.2779166

Masotti, M., Campanini, R., Mazzacurati, L., Falsaperla, S., Langer, H., & Spampinato, S. (2008). TREMOrEC: A software utility for automatic classification of volcanic tremor. *Geochemistry, Geophysics, Geosystems*, *9*(4), Q04007. https://doi.org/10.1029/2007GC001860

Miller, S. A., Collettini, C., Chiaraluce, L., Cocco, M., Barchi, M., & Kaus, B. J. P. (2004). Aftershocks driven by a high-pressure CO_2 source at depth. *Nature*, *427*(6976), 724–727. https://doi.org/10.1038/nature02251

Morabito, S., Cusano, P., Galluzzo, D., Gaudiosi, G., Nardone, L., Del Gaudio, P., et al. (2023). One-year seismic survey of the tectonic CO_2-rich site of Mefite d'Ansanto (Southern Italy): Preliminary insights in the seismic noise wavefield. *Sensors*, *23*(3), 1630. https://doi.org/10.3390/s23031630

Panebianco, S. (2022). Fluid injections in the subsurface: A multidisciplinary approach for better understanding their implications on induced seismicity and the environment. Doctoral Thesis. Retrieved from https://iris.unibas.it/handle/11563/154467

Panebianco, S., Satriano, C., & Stabile, T. A. (2024). ADA: An automated detection algorithm of tremor at Mefite d'Ansanto site (southern Italy) (version 1.0) [Software]. Zenodo. https://doi.org/10.5281/zenodo.10478530

Passarelli, L., Govoni, A., Maccaferri, F., Woith, H., Strollo, A., Zieke, T., et al. (2017). East Pollino Experiment, Southern Italy [Dataset]. GFZ Data Services. Other/SeismicNetwork. https://doi.org/10.14470/LM582526

Pedregosa, F., Varoquaux, G., Gramfort, A., Michel, V., Thirion, B., Grisel, O., et al. (2011). Scikit-learn: Machine learning in Python [Software]. *Journal of Machine Learning Research*, *12*, 2825–2830.

Permana, T., Nishimura, T., Nakahara, H., & Shapiro, N. (2022). Classification of volcanic tremors and earthquakes based on seismic correlation: Application at Sakurajima volcano, Japan. *Geophysical Journal International*, *229*(2), 1077–1097. https://doi.org/10.1093/gji/ggab517

Pischiutta, M., Anselmi, M., Cianfarra, P., Rovelli, A., & Salvini, F. (2013). Directional site effects in a non-volcanic gas emission area (Mefite d'Ansanto, southern Italy): Evidence of a local transfer fault transversal to large NW–SE extensional faults? *Physics and Chemistry of the Earth, Parts A/B/C*, *63*, 116–123. https://doi.org/10.1016/j.pce.2013.03.008

Saccorotti, G., & Lokmer, I. (2021). Chapter 2—A review of seismic methods for monitoring and understanding active volcanoes. In P. Papale, & A. C. Di (Eds.), *Forecasting and planning for volcanic hazards, risks, and disasters* (Vol. 2, pp. 25–73). Elsevier. https://doi.org/10.1016/B978-0-12-818082-2.00002-0

Shapiro, S. A. (2015). *Fluid-induced seismicity*. Cambridge University Press.

Smith, P. J., & Bean, C. J. (2020). RETREAT: A REal-time TREmor analysis tool for seismic arrays, with applications for volcano monitoring. *Frontiers in Earth Science*, *8*. https://doi.org/10.3389/feart.2020.586955

Stabile, T. A., Vlček, J., Wcisło, M., & Serlenga, V. (2021). Analysis of the 2016–2018 fluid-injection induced seismicity in the High Agri Valley (Southern Italy) from improved detections using template matching. *Scientific Reports*, *11*(1), 20630. https://doi.org/10.1038/s41598-021-00047-6

Tamburello, G., Pondrelli, S., Chiodini, G., & Rouwet, D. (2018). Global-scale control of extensional tectonics on CO_2 Earth degassing. *Nature Communications*, *9*(1), 4608. https://doi.org/10.1038/s41467-018-07087-z

The ObsPy Development Team. (2022). ObsPy 1.3.0 (1.3.0) [Software]. Zenodo. https://doi.org/10.5281/zenodo.6327346

ViDEPI Project. (2012). Ministry for economic development DGRME—Italian geological society—Assomineraria. Visibility of petroleum exploration data in Italy. Available online: www.videpi.com (Monte Forcuso 001 well) Retrieved from https://www.videpi.com/videpi/pozzi/dettaglio.asp?cod=3920

Zuccarello, L., De Angelis, S., Minio, V., Saccorotti, G., Bean, C. J., Paratore, M., & Ibanez, J. M. (2022). Volcanic tremor tracks changes in multi-vent activity at Mt. Etna, Italy: Evidence from analyses of seismic array data. *Geophysical Research Letters*, *49*(22), e2022GL100056. https://doi.org/10.1029/2022GL100056

Erratum

In the originally published version of this article, the affiliation for coauthor Claudio Satriano was incorrect. The correct affiliation is Université Paris Cité, Institut de physique du globe de Paris, CNRS, Paris, France. The error has been corrected, and this may be considered the authoritative version of record.